We are IntechOpen,
the world's leading publisher of
Open Access books
Built by scientists, for scientists

4,800
Open access books available

122,000
International authors and editors

135M
Downloads

154
Countries delivered to

Our authors are among the
TOP 1%
most cited scientists

12.2%
Contributors from top 500 universities

CLARIVATE ANALYTICS
BOOK CITATION INDEX
INDEXED

WEB OF SCIENCE™
Selection of our books indexed in the Book Citation Index
in Web of Science™ Core Collection (BKCI)

Interested in publishing with us?
Contact book.department@intechopen.com

Numbers displayed above are based on latest data collected.
For more information visit www.intechopen.com

Sol-Gel Synthesis of Calcium-Deficient Hydroxyapatite: Influence of the pH Behavior during Synthesis on the Structural, Chemical Composition and Physical Properties

José Bruno Rojas Trigos, Yolanda Jiménez-Flores,
Víctor Suárez, Moseratt Suárez-Quezada and
Uriel Nogal

Additional information is available at the end of the chapter

http://dx.doi.org/10.5772/intechopen.76531

Abstract

This work analyzes the influence of the pH on the physical-chemical properties of calcium-deficient hydroxyapatite synthesized by the sol-gel method. The pH evolution in the course of the synthesis was followed during the drop-by-drop adding of the calcium source to the phosphorus source, for different drip rates. The structural, morphological, and textural characterizations demonstrate that increasing the drip rate up to values of 10 $\mu l \cdot s^{-1}$ increases the crystallite size and the specific surface area, while the chemical and optical characterizations show that higher drip rates also increase the calcium and oxygen vacancies, related to an increase in the energy of the optical band gap. However, for the sample synthesized at a drip rate of 17 $\mu l \cdot s^{-1}$, the conjunction of higher calcium and oxygen vacancies has an opposite effect in the optical properties, in comparison to the observations in the synthesized samples at lower drip rates. Finally, the thermal characterization shows that, for all cases, the thermal diffusivity values agree with the reported values elsewhere.

Keywords: chemical composition, hydroxyapatite, optical properties, sol-gel method, thermal properties

1. Introduction

There are many chemical routes for the synthesis of hydroxyapatite and hydroxyapatite compounds, such as biomimetic methods, co-precipitation, and sol-gel methods, among others

IntechOpen

© 2018 The Author(s). Licensee IntechOpen. This chapter is distributed under the terms of the Creative Commons Attribution License (http://creativecommons.org/licenses/by/3.0), which permits unrestricted use, distribution, and reproduction in any medium, provided the original work is properly cited.

[1–3]. It is well known that the characteristics of the synthesis methodology have great influence on the structure, morphology, and chemical composition, as well on the mechanical, thermal, and optical properties of the resultant product. Particularly in the sol-gel synthesis of hydroxyapatite (at normal temperature and pressure conditions), the evolution of the values of the pH during the synthesis strongly affects the final structure and stoichiometry, frequently by promoting the presence of calcium vacancies, crystalline defects, and impurities in the hydroxyapatite structure, modifying the physical-chemical properties of it. While for some applications (e.g., bone replacement and development of bioactive coatings), the presence of high levels of calcium and oxygen deficiencies are undesirable, for other applications such as development luminescent probes and photocatalysts, it are well received and even propitiated [4, 5]. In the year 2006, Degirmenbasi et al. [6] reported a simple sol–gel methodology to obtain stoichiometric hydroxyapatite, by adding drop-by-drop calcium nitrite aqueous solution to sodium phosphate aqueous solution, under mechanical stirring and adjusting the pH at 10, adding sodium hydroxide to the mixture, as needed. Modifying the Degirmenbasi methodology by using a specific amount of sodium hydroxide for the synthesis, Jiménez-Flores et al. [7] reported significant differences in the crystallite size and crystalline fraction, morphology, and thermal properties between samples of calcium-deficient hydroxyapatite, synthesized by using different drip rates and stirring methods (in this case, mechanical and ultrasonic-assisted). In the aforementioned work [7], the observed differences between the synthesized samples were related to an increase in the internal energy during the synthesis—due to the different drip rates and the stirring methods. However, it is also possible that the different drip rates have caused fluctuations in the pH values, affecting the kinetics and the efficiency of the chemical reaction. To clarify the effect of the drip rate in the synthesis of hydroxyapatite, we propose to monitor the evolution of pH during the sol–gel synthesis, comparing the structural, physical, and chemical characteristics of the samples synthesized under different drip rates.

2. Synthesis of calcium-deficient hydroxyapatite

For the sol-gel synthesis of calcium-deficient hydroxyapatite (CDHA), 80 ml of tetra hydrated calcium nitrate ($Ca(NO_3)_2 \cdot 4H_2O$), 48 ml of sodium phosphate (Na_3PO_4), and 16 ml of sodium hydroxide (NaOH) aqueous solutions, at 0.1 M, were prepared at room temperature (25°C). All the chemical compounds were purchased from Sigma-Aldrich.

2.1. Synthesis procedure

The NaOH aqueous solution was incorporated to the $Ca(NO_3)_2 \cdot 4H_2O$ solution and stirred during 30 min to obtain a heterogeneous mixture, as the calcium source. This mixture was then added, drop-by-drop, to the aqueous solution of Na_3PO_4 under continuous stirring at 25°C. During this first stage of the synthesis (**Figure 1**, framed inset), the condensation and gelation of the sol particles take place. To eliminate the solvent (DI water, in this case), the obtained gel is filtered and dried, resulting into a xerogel with the appearance of small brittle glasses. Finally, such glasses were mechanically pulverized obtaining powdered samples of the synthesized compounds. In **Figure 1**, a schematic draw of the CDHA synthesis is shown.

For the purposes of the present work, four different drip rates were used for the CDHA synthesis (see **Table 1**), considering that 20 drops are equivalent to 1 ml.

For each sample, the evolution of the pH during the first stage of the synthesis was followed, making a comparison between the samples during the incorporation of the first 63 ml of the calcium source into the Na_3PO_4 solution. The results are presented in **Figure 2**.

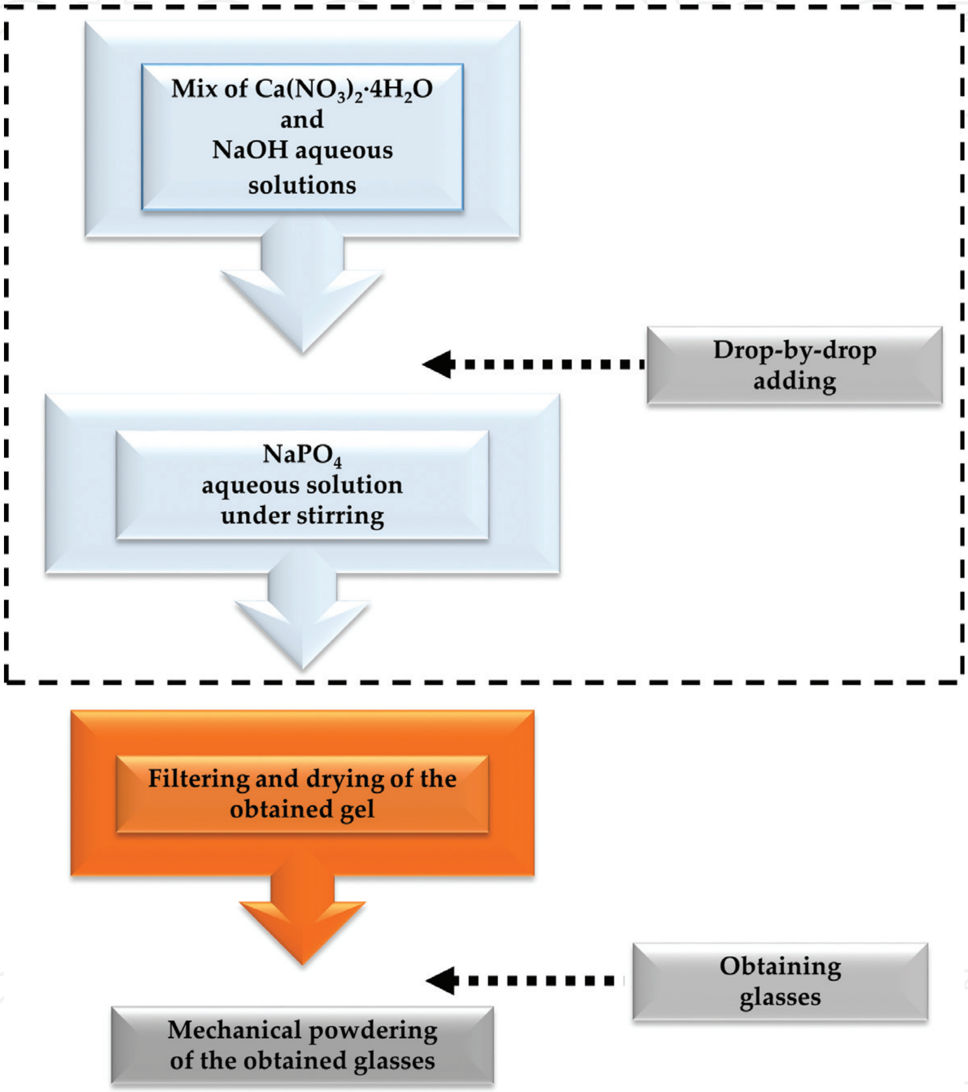

Figure 1. Schematic draw of the sol–gel CDHA synthesis.

Sample	Stirring velocity (rpm)	Drip rate ($\mu l{\cdot}s^{-1}$)	Drying conditions
CDHA_A	600	≈5	24 h at 80°C
CDHA_B		≈8	
CDHA_C		≈10	
CDHA_D		≈17	

Table 1. Parameters employed for the CDHA synthesis.

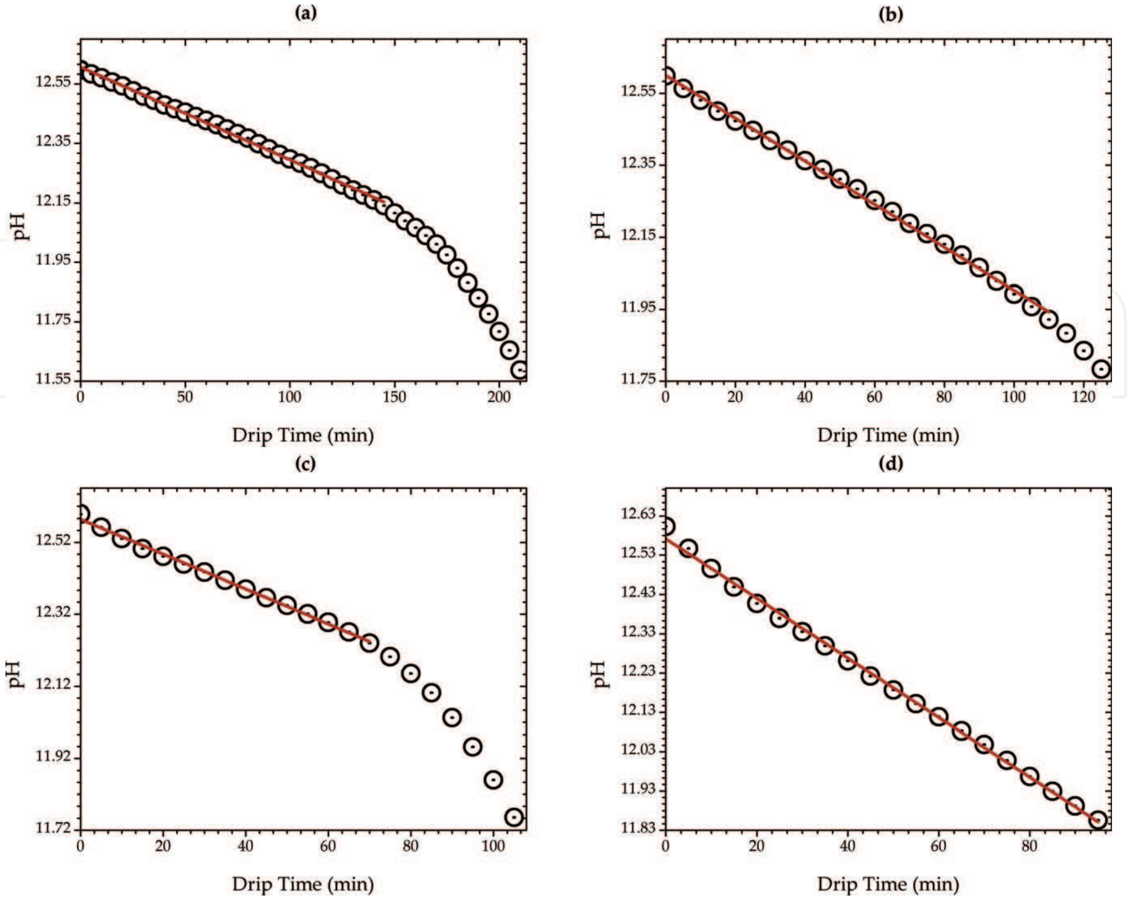

Figure 2. Evolution of the pH during the synthesis of the (a) CDHA_A, (b) CDHA_B, (c) CDHA_C, and CDHA_D samples. The red line represents the best linear fit.

In all cases, the pH values decrease monotonically in time as it was expected; however, the samples exhibit different distinctive features. The shape of drip time vs. pH plots of CDHA_A and CDHA_C samples is quite similar, showing a linear region at the drip beginning (**Figure 2 (a)** and **(c)**), where the pH decreases at rates of 52.2×10^{-6} and 80.8×10^{-6} s^{-1}, respectively. After the linear region, the pH values fall down rapidly changing its concavity, approximately at 2/3 of the drip time for both samples.

On the other hand, the pH values during the synthesis of the CDHA_B sample show a larger linear region than the CDHA_A and CDHA_C samples (**Figure 2(b)**), with a slope of 116.2×10^{-6} s^{-1}; nevertheless, a small concavity change occurs just at the end of the drip time. Contrary to the previous samples, the drip time vs. pH plot of CDHA_D sample (**Figure 2(d)**) shows that the pH values decrease at a constant rate of 126.3×10^{-6} s^{-1}. Finally, it is not worthless to mention that the final pH values (i.e., at the very end of the synthesis of each sample) were 10.04, 11.6, 11.7, and 11.86 for CDHA_A, CDHA_B, CDHA_C, and CDHA_D samples, respectively. This is an important issue to remark, since other authors report that the best conditions for the sol-gel synthesis of stoichiometric hydroxyapatite consider a pH = 10 [6, 8].

3. Structure analysis

3.1. Crystalline structure and surface morphology

By using an X-ray diffractometer (Bruker, D-8 Advance), which employs the Cu-K line (λ = 1.5418 Å) and for diffraction angle ranging $10° \leq \Theta \leq 80°$, the X-ray diffraction pattern was obtained for all samples. The standard corundum powder pattern was used to determine the instrumental width, β_{inst} = 0.047°. In **Figure 3**, the diffraction patterns are displayed identifying the peaks corresponding to the diffraction planes (100), (200), (002), (210), (320), and (004).

The X-ray diffraction patterns agree well (with figure of merit up to 0.9, in all cases) with the ICDD crystallographic chart no. 00–009-0432 (from the International Centre for Diffraction Data database), corresponding to the synthetic hydroxyapatite—with chemical formula, $Ca_5(PO_4)_3(OH)$. For the analysis of the diffraction patterns, the principal observed diffraction peaks were considered to calculate the average crystallite size *D*, by means of the Scherrer equation (Eq. (1)), while the Bragg Law (Eq. (2)) was used for the determination of the unitary cell parameters {*c*, *a*}. In such calculations, the corrected peak width $\beta_c = (\beta^2 - \beta_{inst}^2)^{1/2}$ has been used:

$$D = \frac{0.9\lambda}{\beta_c Cos\Theta} \tag{1}$$

$$\frac{4\,\mathrm{Sin}^2\Theta}{\lambda^2} = \frac{4}{3}\left[\frac{h^2 + hk + k^2}{a^2}\right] + \left[\frac{l}{c}\right]^2 \tag{2}$$

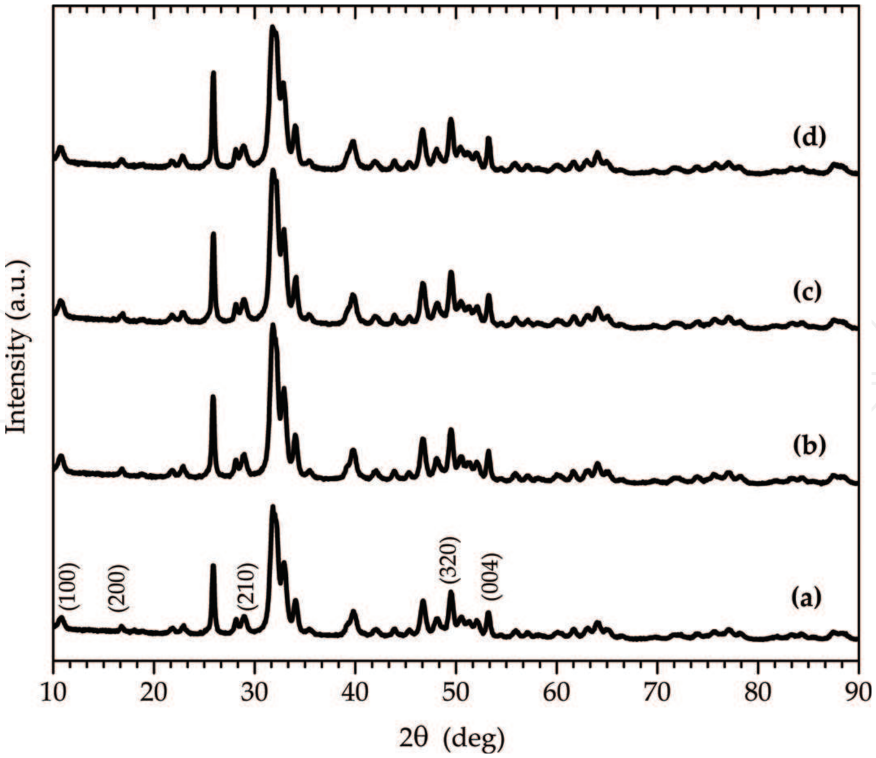

Figure 3. X-ray diffraction patterns of (a) CDHA_A, (b) CDHA_B, (c) CDHA_C, and (d) CDHA_D samples.

In Eq. (2), a hexagonal 6/m-dipyramidal crystal symmetry was considered: being *h*, *k*, and *l* the Miller indexes of the diffraction plane (*h*, *k*, *l*). The results of the analysis has been summarized in **Table 2**, including a comparison with the reported values of unitary cell parameters for stoichiometric hydroxyapatite (c = 6.8745 Å, a = 9.4166 Å) [9].

Although no significant differences were found in the values of the parameters of the unitary cell, a monotonic increase in the crystallite size is observed, as function of the drip rate. The surface morphology of the samples was studied through their corresponding micrographs, taken by a scanning electron microscope, SEM (JEOL, JSM-6390LV), employing an accelerating voltage of 20 kV and a magnification of 20,000× (see **Figure 4**).

Sample	D (Å)	a (Å)	Δa (%)	c (Å)	Δc (%)
CDHA_A	268.3	9.412	0.04	6.877	−0.04
CDHA_B	271.7	9.418	−0.01	6.877	−0.04
CDHA_C	275.3	9.416	0.01	6.875	−0.01
CDHA_D	303.3	9.419	−0.03	6.873	0.02

Table 2. Average crystallite size and unitary cell parameters.

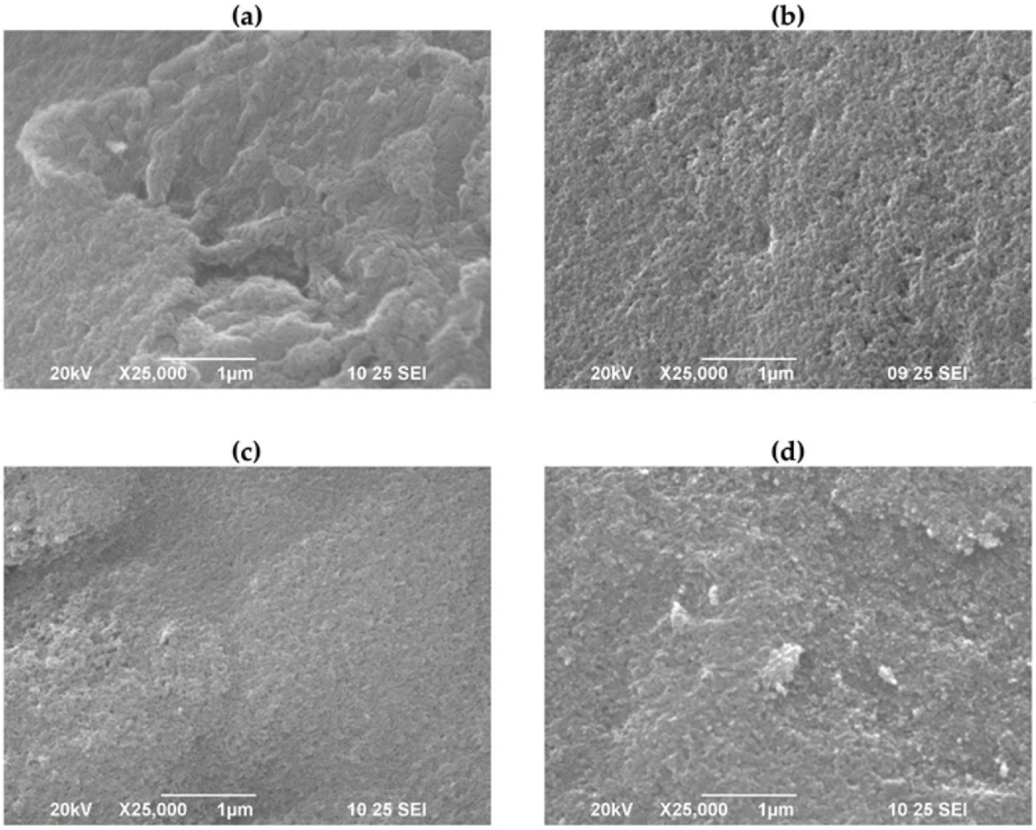

Figure 4. SEM micrographs of samples: (a) CDHA_A, (b) CDHA_B, (c) CDHA_C, and (d) CDHA_D.

The SEM images show that increasing the drip rate has a discernible effect on the surface morphology of the glasses, previously to the mechanical powdering of them. The sample CDHA_A shows the most irregular surface of all (**Figure 4(a)**), small pores being discernible on it, while the sample CDHA_B presents a much more planar surface (**Figure 4(b)**) with (in appearance) larger pores on it. On the other hand, sample CDHA_C shows a less planar but smoother surface (**Figure 4(c)**) and, at least in appearance, a homogenous distribution of small pores on the surface. The case of CDHA_D presents a compact and granulated surface (**Figure 4(d)**), but still small pores are perceived.

IntechOpen

3.2. Textural properties

In order to determine the textural properties of the synthesized samples, the adsorption isotherms for 100 mg of powdered samples were obtained (see **Figure 5**) employing a Quantachrome NOVA4200e equipment, using N_2 as adsorbate. The measurement temperature was kept at $-196°C$, using liquid nitrogen as coolant.

From the adsorption isotherms, the specific surface area was determined by the Brunauer-Emmett-Teller (BET) method, while the Barrett-Joyner-Halenda (BJH) method was for the determination of the pore size diameter [10, 11]. The textural properties of the samples have

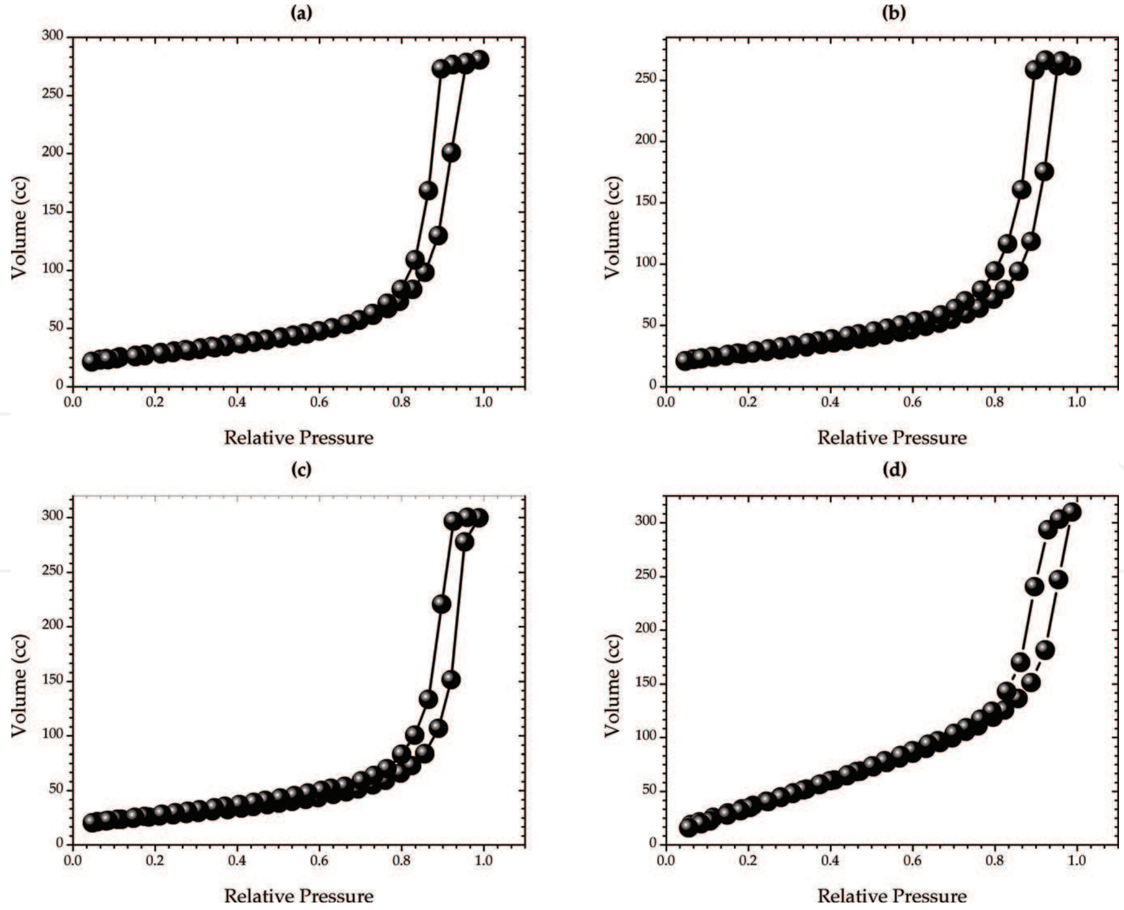

Figure 5. Adsorption isotherms of (a) CDHA_A, (b) CDHA_B, (c) CDHA_C, and (d) CDHA_D samples.

Sample	Specific surface area ($m^2 \cdot g^{-1}$)	Pore size diameter (Å)	Total pore volume ($cm^3 \cdot g^{-1}$)
CDHA_A	101.860	203.2	0.434
CDHA_B	91.856	212.9	0.464
CDHA_C	96.178	181.9	0.405
CDHA_D	92.403	117.2	0.391

Table 3. Textural properties of the studied samples.

been summarized in **Table 3**. From their shape, the isotherms shown in **Figure 5** can be classified as type V isotherm, which indicates unrestricted multilayer adsorption, characteristic of mesoporous materials. The shape of the hysteresis loops is indicative of ink-bottle-shaped pores, associated to poor network connectivity effects [12].

The textural properties agrees well with the SEM observations, correcting the initial visual impression on the pore size on the surface of the samples. With the exception of the CDHA_A sample, the pore radius size, as well as the total pore volume, decreases with increasing drip rate.

4. Chemical characterization

4.1. Elemental chemical composition

The elemental chemical composition was determined using an energy-dispersive X-ray spectroscopy (EDS) system, integrated to the SEM equipment, which employs a Si-Li detector (Oxford Pentafet, mod. 7582). From the EDS spectra recorded for energies ranging 0.12–12 keV, the elemental quantification, as well as the Ca/P and the (Ca + O)/P ratios, has been determined and summarized in **Table 4**.

The results of the elemental quantification by EDS, together with the pH behavior during the synthesis, are indicative that the mass flow (controlled through the drip rate) significantly affects the reaction kinetics during the formation of hydroxyapatite, influencing the efficiency of ion exchange, promoting calcium and oxygen vacancies. The values of carbon content in the samples are consistent with the observed surface morphology and textural properties at different drip rates, suggesting the hypothesis that the presence of carbon in the samples could be due to the absorption of atmospheric CO_2.

Sample	Na (at.%)	C (at.%)	O (at.%)	P (at.%)	Ca (at.%)	Ca/P	(Ca + O)/P
CDHA_A	—	9.78	54.58	13.87	21.77	1.57	5.50
CDHA_B	—	7.40	56.91	14.56	21.13	1.45	5.36
CDHA_C	—	6.53	57.69	14.79	20.99	1.42	5.32
CDHA_D	0.21	8.59	57.32	14.42	19.46	1.35	5.32

Table 4. Quantification of the elemental chemical composition of the samples.

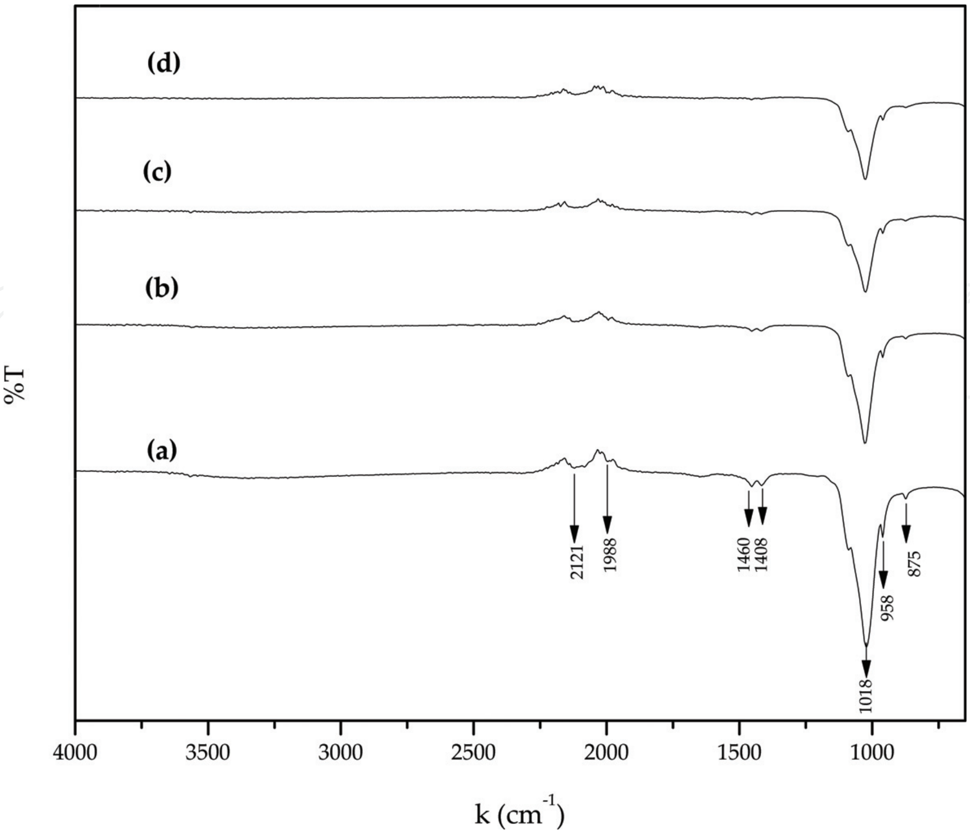

Figure 6. FTIR spectra of samples: (a) CDHA_A, (b) CDHA_B, (c) CDHA_C, and (d) CDHA_D.

4.2. Functional groups detected

For the identification of the functional groups present in samples, the diffuse reflectance spectra were obtained using a FTIR spectrophotometer (Shimadzu, IR Affinity-1S), operating in the attenuated total reflection mode, and the spectroscopic wave number ranging 4000 cm^{-1} $\leq k \leq$ 650 cm^{-1}. At next (**Figure 6**), the FTIR spectra are displayed identifying the detected signals.

The signals centered at 958 and 1018 cm^{-1} are typical of asymmetric stretching of P—O bond of the PO_4^{-3} functional group, while the signal at 875 cm^{-1} corresponds also to the P—O asymmetric stretch but for the HPO_4^{-2} functional group. The signals in the neighborhood of 1408 and 1460 cm^{-1} correspond to stretching of the C—O bond, proper of the inorganic carbonate group. Finally, the signals at 2121 and 1988 cm^{-1} are related to the symmetrical stretching of the H—P bond in the HPO_4^{-2} functional group. These results agree with the EDS elemental quantification and the X-ray diffraction patterns, confirming the formation of calcium-deficient hydroxyapatite. In addition, the presence of carbonate signals supports the hypothesis that the carbon content is due to the atmospheric CO_2 absorbed during the synthesis.

5. Optical properties

To investigate on the optical properties of the CDHA samples (particularly the optical band gap), two experimental techniques were employed here: the UV–Vis spectroscopy and the photoacoustic spectroscopy (PAS) techniques. The UV–Vis technique provides the diffuse reflectance, characterized by the Kubelka-Munk function F(R), as function of the wavelength (equivalent to the photon energy) of the excitation beam. Since the F(R) function depends linearly on the ratio between the optical absorption and the scattering coefficients, an empirical estimation of the band gap, E_g, is possible by extrapolation of the linear region of the Tauc plots [13]. However, the UV–Vis technique is quite sensitive to light scattering effects, so, an over estimation of E_g value is frequent. On the other hand, the PAS technique directly provides the optical absorption spectra, being less disturbed by light scattering effects than other optical spectroscopic techniques, because the PAS signal is generated only by the internal heat diffusion in the sample, as result by the optical absorption and the non-radiative thermal relaxation mechanisms [14, 15].

5.1. UV–Vis diffuse reflectance spectra

A UV–Vis spectrophotometer (Agilent, mod. Cary-100) was employed to measure the F(R) spectrum of the synthesized samples, ranging the wavelength from 200 nm ≤ λ ≤ 250 nm, correcting the obtained spectrums by measuring the background signal. In **Figure 7**, the Tauc plots, from the F(R) values, are exhibited considering the samples as indirect band gap materials.

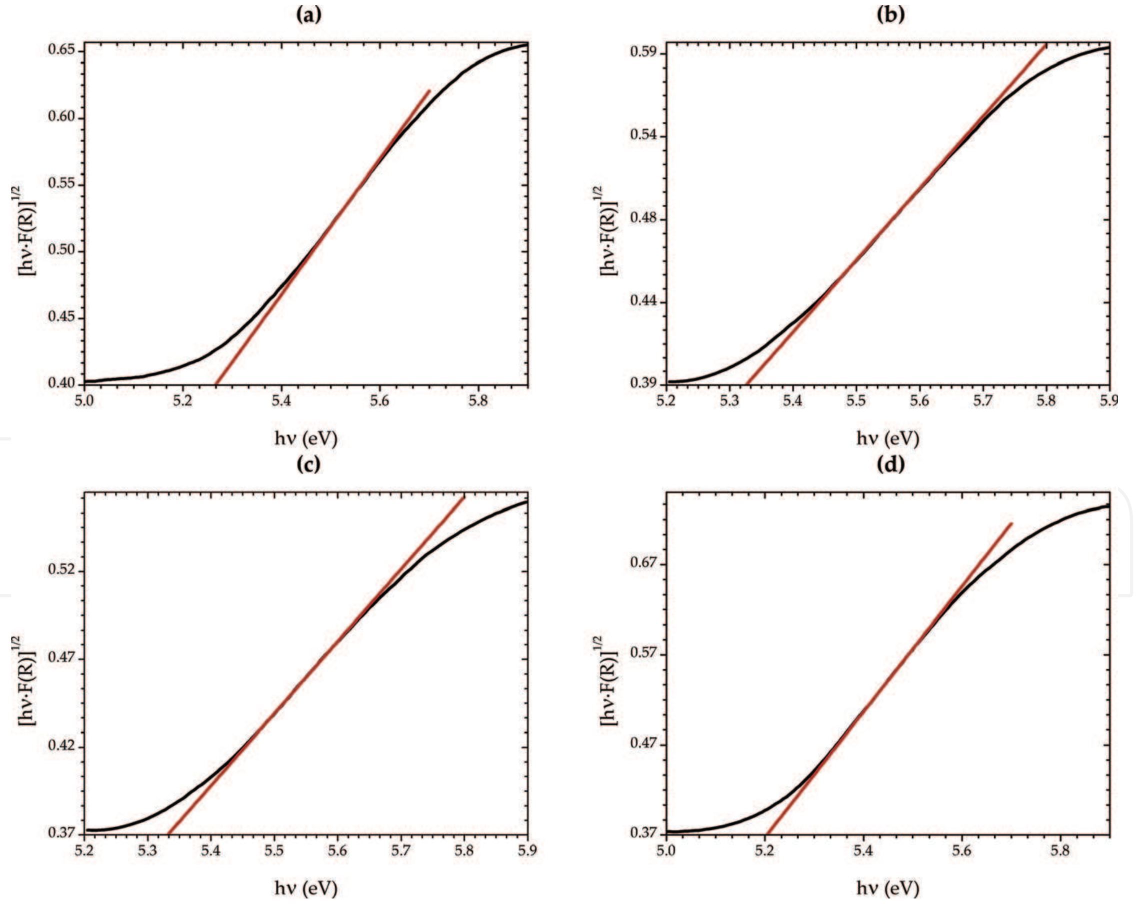

Figure 7. Tauc plots of (a) CDHA_A, (b) CDHA_B, (c) CDHA_C, and (d) CDHA_D samples. The red line shows the extrapolation of the linear region.

5.2. PAS absorption spectra

To record the absorption spectra of the samples, a homemade PAS measurement system was used for such goal, for a wavelength ranging 206 nm $\le \lambda \le$ 288 nm and for a modulation frequency f = 17 Hz. A schematic drawing of the experimental setup is presented as follows (**Figure 8**).

The continuous beam, emitted by the 200 W Hg Arc lamp (Newport, Mod. 66,483) optimized for UV, passes through a monochromator (Newport, mod. Cornerstone 130 1/8 m) to obtain a quasi-monochromatic excitation beam. The continuous excitation beam was then modulated by a mechanical chopper (Stanford Research Systems, mod. SR-540), impinging into the optical window of the PAS measurement cell (MTEC, mod. 300). The PAS signal (**S**, $\Delta\phi$) was then filtered and amplified by a lock-in amplifier (Stanford Research Systems, mod. SR 830), using the modulation frequency as reference, to be storage for its further analysis. From the absorption spectra, the Tauc plots of the samples were constructed for the empirical determination of the optical band gap energies (**Figure 9**).

The optical band gap calculations, from UV–Vis and PAS measurements, are reported in **Table 5**, for purposes of comparison between techniques.

As can be seen from the above results, as the drip rate gets higher, the energy band gap also increases, with the one exception of the CDHA_D, and as it was expected, there is an overestimation on the optical band gap calculations from UV–Vis data. Nevertheless, in both cases (and for all samples) the empirical determination of E_g agrees with the reported values for hydroxyapatite from UV–Vis measurements and density functional theory (DFT) calculations [16, 17]. Using atomistic calculations, Santos and Rezende [18] conclude that the formation of the most probable defects in hydroxyapatite always involves calcium and oxygen vacancies, in agreement to the DFT calculations reported by de Leeuw et al. [19] and de Leeuw [20]. Based on the previous works in the EDS quantification, the increasing of the E_g is

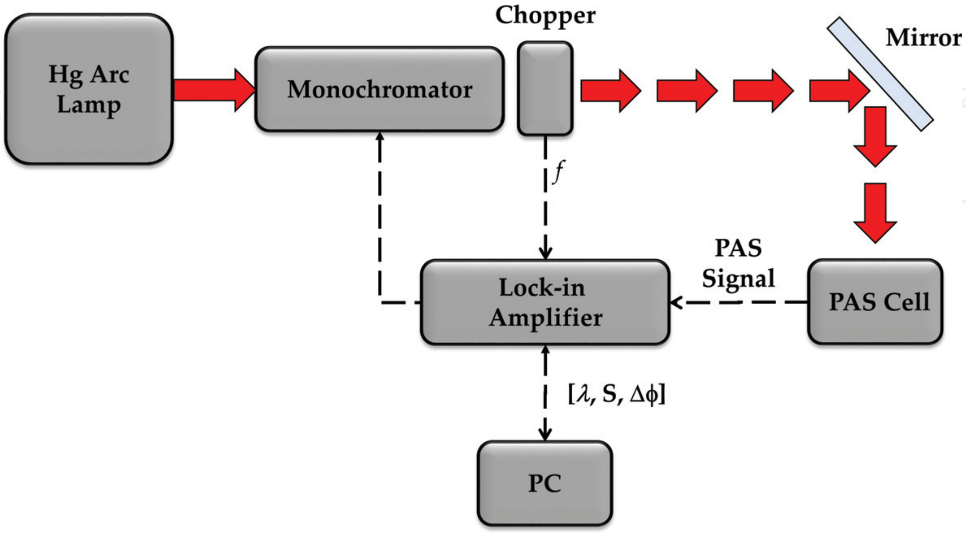

Figure 8. PAS measurement system. Here, **S** and $\Delta\phi$ are the amplitude and the phase shift of the PAS signal, respectively.

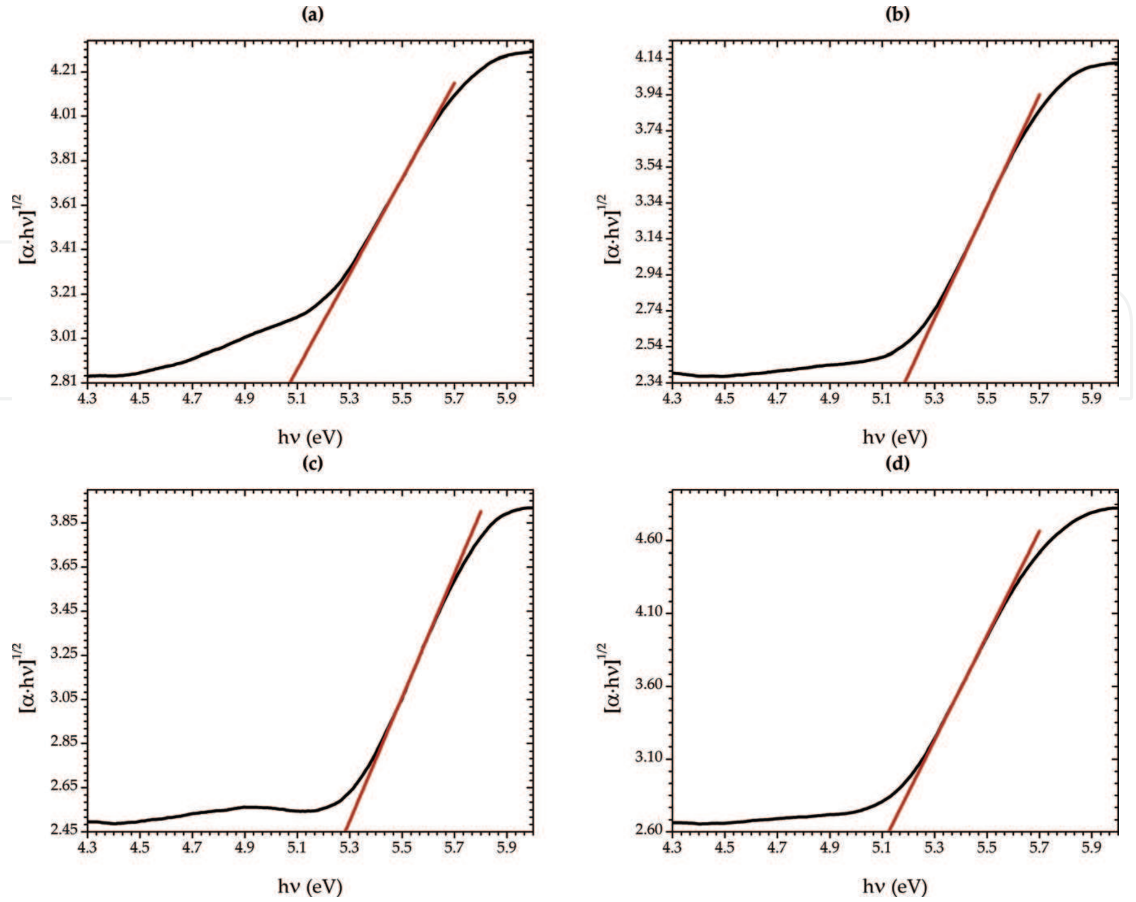

Figure 9. Tauc plots of (a) CDHA_A, (b) CDHA_B, (c) CDHA_C, and (d) CDHA_D samples. The red line shows the extrapolation of the linear region.

Sample	$E_g{}^a$ (eV)	$E_g{}^b$ (eV)	ΔE_g (%)
CDHA_A	5.26	5.1	3.14
CDHA_B	5.31	5.18	2.51
CDHA_C	5.33	5.29	0.76
CDHA_D	5.21	5.12	1.76

[a] From UV-Vis.
[b] From PAS.

Table 5. Optical band gap values determined from UV–Vis and PAS measurements.

IntechOpen

explained as an effect mostly due to a higher levels of calcium and oxygen (in the OH sites) vacancies, as the drip rate increases from 5 to 10 μl·s^{-1}. For a higher drip rate (i.e., 17 μl·s^{-1}), it is possible that the oxygen vacancies occur at the phosphate sites as well at the OH sites. In such case, the DFT calculations predict the existence of energy levels inside the forbidden band, which explains why the band gap energy decreases for the CDHA_D sample.

6. Thermal properties

For the determination of the thermal response of the samples, a homemade photoacoustic detection (PA) measurement system was employed, for a modulation frequency ranging 400 Hz ≤ f ≤ 4 kHz. The experimental setup is similar to the PAS measurement system but replacing the Hg arc lamp and the monochromator by a 405 nm laser diode (controlled by a TTL signal), as is shown in **Figure 10**.

The excitation beam wavelength was chosen to avoid the contribution of the photogenerated charge carriers to the PA signal. To perform the PA measurements in the transmission configuration [21, 22], pills of powdered samples were obtained by compacting 100 mg of powdered sample. Considering the samples as optically opaque and thermally thick, the PA signal will depend on the modulation frequency as indicated by Eq. (3):

$$S = A_0 \cdot \frac{\exp\left(-\sqrt{f/f_c}\right)}{f}; \qquad f_c \equiv \frac{\alpha_s}{\pi \cdot l_s^2} \tag{3}$$

In Eq. (3), A_0 is an instrumental constant, f_c is the so-called characteristic frequency of the sample, and α_s and l_s are the thermal diffusivity and thickness of the sample, respectively. For modulation frequencies where Eq. (3) is applicable, α_s can be calculated from the slope of the linear region in the semi-logarithmic $f^{1/2}$ vs. $f{\cdot}\mathbf{S}$ plot (**Figure 11**). The results obtained have been summarized in **Table 6**.

Although the values of the thermal diffusivities agree with the reported values for hydroxyapatite [7, 23, 24], there is no clear correlation with the synthesis drip rate nor the stoichiometry of the samples. This is because the different levels of compaction of the sample's pills affect the effective thermal properties. The nonlinear behavior at low modulation frequencies is

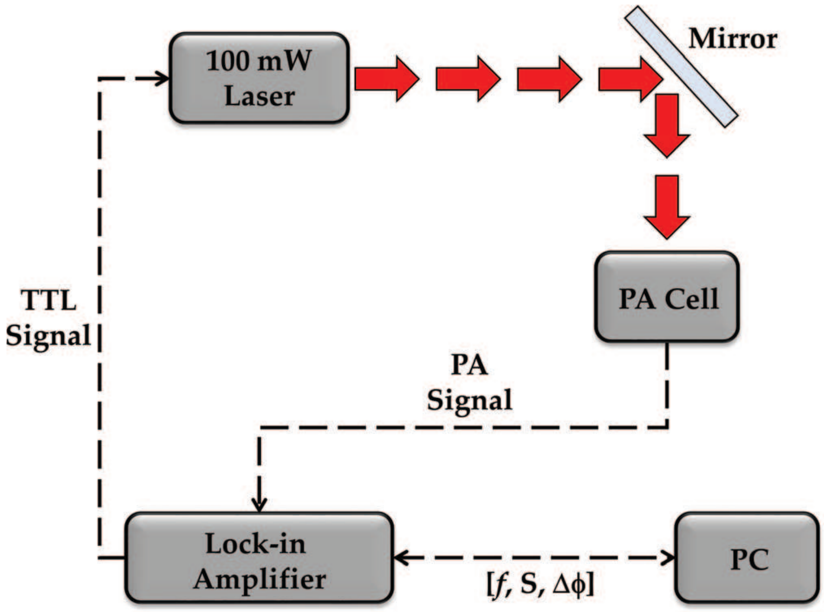

Figure 10. PA measurement system. Here, **S** and Δϕ are the amplitude and the phase shift of the PA signal, respectively.

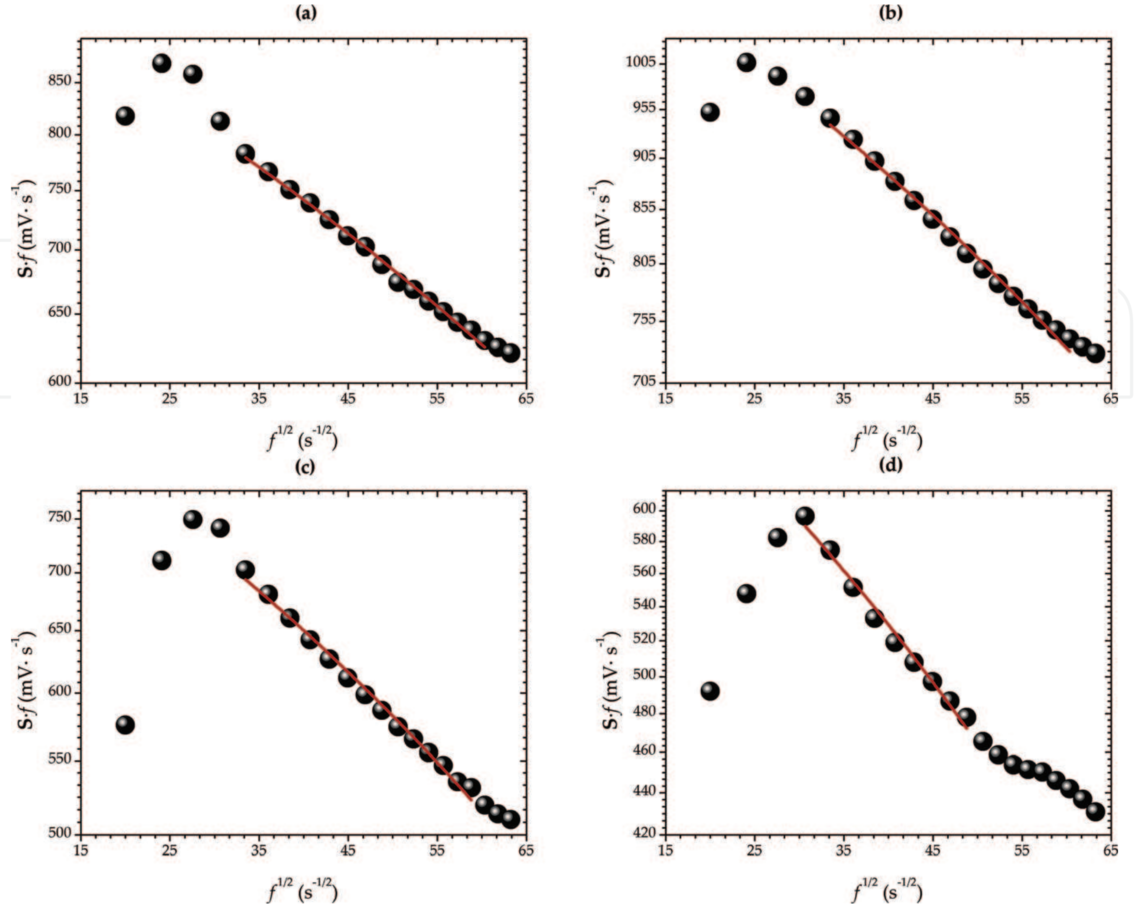

Figure 11. $f^{1/2}$ vs. f·S plot of (a) CDHA_A, (b) CDHA_B, (c) CDHA_C, and (d) CDHA_D. The red line shows the best fit.

Sample	Slope (mV·$s^{-1/2}$)	f_c ($\times 10^{-3}$ Hz)	α_s ($\times 10^{-7}$ $m^2 \cdot s^{-1}$)
CDHA_A	−5.75	30.29	1.90
CDHA_B	−7.78	16.53	1.02
CDHA_C	−6.75	21.93	2.42
CDHA_D	−6.49	23.73	2.58

Table 6. Thermal diffusivity of the samples.

indicative of a transition between thermal regimes. For larger modulations frequencies, the signal-to-noise ratio becomes too small (especially for CDHA_D sample) to obtain reliable data. The previous results must be corroborated by other photothermal techniques, such as IR photothermal radiometry or lock-in thermography [25, 26].

7. Conclusions

The sol–gel synthesis of calcium-deficient hydroxyapatite was successfully achieved, for four different drip rates during synthesis procedures, describing the distinctive features of the pH evolution, for each case. For the samples synthesized at drip rate values of 5, 8, 10, and

17 μl·s^{-1}, the structural, morphological, and textural characterizations show that the pore radius size and the total pore volume tend to decrease for a drip rate up to 5 μl·s^{-1}, contrary to the crystallite size, which decreases for all samples as the drip rate increases. The chemical characterizations demonstrate that increasing the drip rate promotes the presence of calcium and oxygen vacancies in the hydroxyapatite structure. From the diffuse reflectance and absorbance spectra, the energy band gap of the samples increases as the drip rate does, with the exception of the sample synthesized at 17 μl·s^{-1}, possible due to a combination of a larger presence of oxygen vacancies on the phosphate sites and calcium vacancies. The results of the thermal characterization allowed determining the effective thermal diffusivity of the samples, obtaining values that agree well with those reported in the literature. However, it was not possible to establish a clear correlation between the effective thermal properties and the values of the drip rate used during the synthesis. Finally, the drip rate in the hydroxyapatite sol-gel synthesis clearly governs the pH during synthesis and, therefore, has a major impact in the physical-chemical properties of the hydroxyapatite.

Acknowledgements

Authors acknowledge the Instituto Politécnico Nacional from Mexico, for financial support through 1855 SIP multidisciplinary and 20170229 SIP projects. The authors wish to thank the National Energy Conversion and Storage Laboratory, CICATA U. Legaria of the Instituto Politécnico Nacional of Mexico, and the PhD student René Cabrera for helping with the acquisition and analysis of XRD data. The authors thank also the PhD student Guadalupe Romero Ortiz for helping in the acquisition of hydrogen adsorption data.

Conflict of interest

The authors of this work declare no conflicts of interest of any kind.

Author details

José Bruno Rojas Trigos[1]*, Yolanda Jiménez-Flores[1], Víctor Suárez[2], Moseratt Suárez-Quezada[1] and Uriel Nogal[3]

*Address all correspondence to: jrojast@ipn.mx

1 Instituto Politécnico Nacional, Centro de Investigación en Ciencia Aplicada y Tecnología Avanzada, Unidad Legaria, Ciudad de México, Mexico

2 Cátedras CONACYT, Departamento de Química, ECOCATAL, Universidad Autónoma Metropolitana-Iztapalapa, Ciudad de México, Mexico

3 Cátedras CONACYT, Instituto Politécnico Nacional, Centro de Investigación en Ciencia Aplicada y Tecnología Avanzada, Ciudad de México, Mexico

References

[1] Supová M. Substituted hydroxyapatites for biomedical applications: A review. Ceramics International. 2015;**41**:9203-9231. DOI: 10.1002/jbm.b.33651

[2] Ferraz MP, Monteiro FJ, Manuel CM. Hydroxyapatite nanoparticles: A review of preparation methodologies. Journal of Applied Biomaterials and Biomechanics. 2004;**2**:74–80. ISSN: 1722-6899

[3] Nasser Mostafa Y. Characterization, thermal stability and sintering of hydroxyapatite powders prepared by different routes. Materials Chemistry and Physics. 2005;**94**:333-341. DOI: 10.1016/j.matchemphys.2005.05.011

[4] Deshmukh K, Shaik MM, Ramanan SR, Kowshik M. Self-activated fluorescent hydroxyapatite nanoparticles: A promising agent for bioimaging and biolabeling. ACS Biomaterials Science & Engineering. 2016;**2**:1257-1264. DOI: 10.1021/acsbiomaterials.6b00169

[5] Rosenmana G, Aronova D, Oster L, Haddad J, Mezinskis G, Pavlovska I, Chaikina M, Karlov A. Photoluminescence and surface photovoltage spectroscopy studies of hydroxyapatite nano-bio-ceramics. Journal of Luminescence. 2007;**122-123**:936-938. DOI: 10.1016/j.jlumin.2006.01.331

[6] Degirmenbasi N, Kalyon DM, Birinci E. Biocomposites of nanohydroxyapatite with collagen and poly(vinyl alcohol). Colloids and Surfaces B: Biointerfaces. 2008;**48**:42-49. DOI: 10.1016/j.colsurfb.2006.01.002

[7] Jiménez-Flores Y, Camacho N, Rojas-Trigos JB, Suárez M. Synthesis and thermal characterization of hydroxyapatite powders obtained by sol-gel technique. In: Campos RP, Cuevas AC, Esparza Muñoz RA, editors. Characterization of Metals and Alloys. Switzerland: Springer International Publishing; 2017. pp. 167-180. DOI: 10.10071978-3-319-31694-9_14

[8] Mollazadeh S, Javadpour J, Khavandi A. In situ synthesis and characterization of nanosize hydroxyapatite in poly(vinyl alcohol) matrix. Ceramics International. 2007;**33**:1579-1583. DOI: 10.1016/j.ceramint.2006.06.006

[9] Bideaux RA, Bladh KW, Nichols MC. In: Anthony JW, editor. Handbook of Mineralogy: Arsenates, Phosphates, Vanadates. Vol. 4. Chantilly, VA, USA: Mineralogical Society of America; 2000

[10] Brunauer S, Emmett PH, Teller E. Adsorption of gases in multimolecular layers. Journal of the American Chemical Society. 1938;**60**(2):309-319. DOI: 10.1021/ja01269a023

[11] Barret PB, Joyner LG, Halenda PP. The determination of pore volume and area distributions in porous substances. I. Computations from nitrogen isotherms. Journal of the American Chemical Society. 1951;**73**(1):373-380. DOI: 10.1021/ja01145a126

[12] Sing KSW, Everett DH, Haul RAW, Moscou L, Pierotti RA, Rouquérol RJ, Siemieniewska T. Reporting physisorption data for gas/solid systems with special reference to the

determination of surface area and porosity. Pure and Applied Chemistry. 1985;**57**(4):603-619. DOI: 10.1351/pac198557040603

[13] Tauc J. Optical properties and electronic structure of amorphous Ge and Si. Materials Research Bulletin. 1968;**3**:37-46. DOI: 10.1016/0025-5408(68)90023-8

[14] Rosencwaig A. Theoretical aspects of photoacoustic spectroscopy. Journal of Applied Physics. 1978;**49**:2905-2910. DOI: 10.1063/1.325175

[15] McDonald FA, Wetsel GC. Generalized theory of the photoacoustic effect. Journal of Applied Physics. 1978;**49**:2313-2322. DOI: 10.1063/1.325116

[16] Piccirillo C, Dunnill CW, Pullar RC, Tobaldi DM, Labrincha JA, Parkin IP, Pintado MM, Castro PML. Calcium phosphate-based materials of natural origin showing photocatalytic activity. Journal of Materials Chemistry A. 2013;**1**(21):6452-6461. DOI: 10.1039/C3TA10673J

[17] Bystrov VS, Piccirillo C, Tobaldi DM, Castro PML, Coutinho J, Kopyl S, Pullar RC. Oxygen vacancies, the optical band gap (Eg) and photocatalysis of hydroxyapatite: Comparing modelling with measured data. Applied Catalysis B: Environmental. 2016;**196**:100-107. DOI: 10.1016/j.apcatb.2016.05.014

[18] Santos RDS, Rezende MVS. Atomistic simulation of intrinsic defects and trivalent and tetravalent ion doping in hydroxyapatite. Advances in Condensed Matter Physics. 2014;**2014**:609024. DOI: 10.1155/2014/609024

[19] de Leeuw NH, Bowe JR, Rabone JAL. A computational investigation of stoichiometric and calcium-deficient oxy-deficient hydroxyl-apatites. Faraday Discussions. 2007;**134**:195-214. DOI: 10.1039/b602012g

[20] de Leeuw NH. Computer simulations of structures and properties of the biomaterial hydroxyapatite. Journal of Materials Chemistry. 2010;**20**:5376-5389. DOI: 10.1039/b921400c

[21] Rosencwaig A, Gersho A. Theory of the photoacoustic effect with solids. Journal of Applied Physics. 1976;**47**:64-69. DOI: 10.1063/1.322296

[22] Almond D, Patel P. Photothermal Sciences and Techniques. 1st ed. Devon: Chapman & Hall; 1996. p. 119. ISBN: 0 412 57880 8

[23] Coelho TM, Nogueira ES, Weinand WR, Lima WM, Steimacher A, Medina AN, Baesso ML, Bento AC. Thermal properties of natural nanostrunctured hydroxyapatite extracted from fish bone waste. Journal of Applied Physics. 2007;**101**:084701. DOI: 10.1063/1.2718866

[24] Calderón A, Peña Rodríguez G, Muñoz Hernández RA, Díaz Góngora JAI, Mejía Barradas CM. Thermal diffusivity in bone and hydroxyapatite. In: Vargas-Luna M, editor. Medical Physics: Eighth Mexican Symposium on Medical Physics; Guanajuato, Gto, Mexico. Melville, NY: AIP Publishing; 2004. pp. 278-281

[25] Martínez K, Marín E, Glorieux C, Lara-Bernal A, Calderón A, Peña Rodríguez G, Ivanov R. Thermal diffusivity measurements in solids by photothermal infrared radiometry:

Influence of convection-radiation heat losses. International Journal of Thermal Sciences. 2015;**98**:202-207. DOI: 10.1016/j.ijthermalsci.2015.07.019

[26] Bissieux C, Pron H, Henry JF. Photothermal and thermomechanical infrared thermography. In: Moares EM, editor. Thermal Wave Physics and Related Photothermal Techniques: Basic Principles and Recent Developments. Transworld Research Network; 2009. pp. 253-285. ISBN: 978-81-7895-401-1

IntechOpen

IntechOpen